

Electronic Supplementary Information for

Modulation of Electron Distribution and Intermediates Adsorption by C–O–Si Sites for Efficient Oxygen Reduction and Lithium Storage

Shouhua Yang,^{‡a} Ying Tang,^{‡a} Zhen Yang,^{‡a} Shengchao Yang,^{*a} Boqin Li,^a Wencai Peng,^a Banghua Peng,^a Gang Wang,^a Jie Liang,^c Junyi Ji,^{*b} Feng Yu,^{*ad}

^a Key Laboratory for Green Processing of Chemical Engineering of Xinjiang Bingtuan, School of Chemistry and Chemical Engineering, Shihezi University, Shihezi 832003, China

^b College of Chemical Engineering, Sichuan University, Chengdu, Sichuan 610065, P. R. China

^c School of Energy and Power Engineering, Beihang University, Beijing 102206, China

^d Carbon Neutralization and Environmental Catalytic Technology Laboratory, Bingtuan Industrial Technology Research Institute, Shihezi University, Shihezi 832003, China

[‡]These three authors contributed equally to this work.

***Corresponding authors:**

shengchao.yang@shzu.edu.cn (S. Yang)

junyiji@scu.edu.cn (J. Ji)

yufeng05@mail.ipc.ac.cn (F. Yu)

Supplementary Experimental Section

Preparation of Si-doped carbon catalysts

To prepare Si-doped carbon catalysts, 1.0 g of banana peel powder was dissolved in 3 mL of N-methyl-2-pyrrolidinone (NMP) and stirred for 30 min at room temperature. Next, 1.2 mL of SiCl₄ was added dropwise to the stirred solution. Once the reaction was complete, the mixture was transferred to a household microwave oven and heated at medium-high heat (700 W) for 5 min to dry the solution. The resulting solid composite was then transferred to a tube furnace and heated in an argon atmosphere at a rate of 5°C/min to 900°C, where it was maintained for 3 h to obtain Si-BP-Carbon.

For comparison, BP-Carbon was also fabricated using the same procedure without adding SiCl₄. The supporting information details sample characterization, oxygen reduction reaction (ORR) performance testing, theoretical calculations, and lithium-ion battery performance testing.

Sample characterization

The surface morphology of the materials was characterized via scanning electron microscopy (SEM; Hitachi SU 8020). Transmission electron microscopy (TEM; FEI Tecnai G2 F30) was employed to analyze the elemental distribution of the material surface, providing detailed information on the microscopic morphology and internal structure. Energy-dispersive X-ray spectroscopy spectra were obtained using an X-ray energy spectrometer (HORIBA EX-250). The aqueous static contact angle of the catalysts was measured using a contact angle meter (Kruss DSA100). X-ray diffraction (XRD; D8 ADVANCE) was employed to investigate the degree of graphitization and surface defects. Concurrently, Raman spectroscopy (Renishaw InVia) was employed to evaluate the degree of graphitization and crystal structure. Fourier transform infrared (FT-IR, Nicolet 6700) spectroscopy analyzed the molecular structure and function groups of the catalysts. X-ray photoelectron spectroscopy (XPS; ESCALAB 250Xi) determined the surface elemental composition and bonding states of the catalysts. The surface area, pore volume, and pore size were determined using the Brunauer–Emmett–Teller (BET; TriStar II 3020) method. Finally, structures and compositions of the samples were investigated via solid-state nuclear magnetic resonance (Bruker AVANCE III 600M) characterization.

ORR performance testing

The ORR activity of the catalysts was characterized using an electrochemical workstation (CHI 760E) equipped with a standard three-electrode system. An oxygen-saturated 0.1 M KOH solution was used as the electrolyte. Carbon rods served as auxiliary electrodes, Ag/AgCl (saturated KCl) electrodes were employed as reference

electrodes, and glassy carbon disk electrodes coated with catalysts (RDE; $d = 3$ mm) were used as working electrodes. The catalyst ink was prepared by dispersing 5 mg of the samples in a mixture of 500 mL of ethanol, 500 mL of ultrapure water, and 25 μL of Nafion solution (5 wt%), followed by ultrasonic dispersion for 1 h until a homogeneous suspension was formed. A working electrode was prepared by depositing 15 μL of the catalyst ink onto the surface of a polished glassy carbon electrode and allowing it to air-dry, resulting in a loading of $1.04 \text{ mg}\cdot\text{cm}^{-2}$. Cyclic voltammetry (CV) and linear scanning voltammetry (LSV) curves were recorded at a $5 \text{ mV}\cdot\text{s}^{-1}$ scanning rate. LSV curves were obtained at various rotational speeds (400-2500 rpm), and the resulting current densities were normalized based on the geometric area of the glassy carbon electrode. The stability of the catalysts was evaluated using a timed current method in a 0.1 M KOH solution at 625 rpm for 30,000 s. Methanol tolerance experiments were performed by adding 1 mL of methanol and assessing the stability over 1500 s under the same conditions. The accelerated degradation tests (ADT) were performed by cycling between 0.6 and 1.0 V. All end potentials were referenced using a reversible hydrogen electrode (RHE) throughout the experiments.

The electrochemical surface area (ECSA) of the catalyst is evaluated by comparing its specific double layer capacitance (C_{dl} , $\text{mF}\cdot\text{cm}^{-2}$). Under identical test conditions, the ECSA is positively correlated with the C_{dl} of the material. In the non-Faradaic region, CV curves were measured at different scan rates ($v = 2, 4, 6, 8, 10, 12 \text{ mV}\cdot\text{s}^{-1}$). The relationship between the measured capacitive current density (Δj , $\text{mA}\cdot\text{cm}^{-2}$), v and C_{dl} is expressed as follows:

$$\Delta j = j_{anodic} - j_{cathodic} = 2vC_{dl} \quad (1)$$

The number of electrons transferred (n) for the ORR was calculated using the Koutecky-Levich (K-L) equation:

$$1/J = 1/J_k + 1/J_L = 1/J_k + 1/(B\omega^{1/2}), \quad (2)$$

where J denotes the current density measured at the RDE and J_k and J_L represent the charge transfer kinetics and diffusion-limited current density, respectively. ω is the electrode's angular velocity, and B is defined using the following equation:

$$B = 0.2nFC_0D_0^{2/3}v^{-1/6}, \quad (3)$$

where n denotes the number of electrons transferred per molecule of O_2 during the ORR, F is $96485 \text{ C}\cdot\text{mol}^{-1}$ (Faraday's constant), C_0 is $1.2 \times 10^{-3} \text{ mol}\cdot\text{L}^{-1}$ (dissolved O_2 concentration), D_0 is $1.9 \times 10^{-5} \text{ cm}^2\cdot\text{s}^{-1}$ (O_2 diffusion coefficient), and v is $0.01 \text{ cm}^2\cdot\text{s}^{-1}$ (electrolyte kinematic viscosity).

The hydrogen-peroxide current response was tested using a rotating RDE (RRDE). The hydrogen-peroxide yield ($\text{H}_2\text{O}_2\%$) and number of electrons transferred (n) were

calculated using the following equations:

$$\text{H}_2\text{O}_2(\%) = 200 * \frac{I_r/N}{I_d + I_r/N}, \quad (4)$$

$$n = 4 * \frac{I_d}{I_d + I_r/N}, \quad (5)$$

where I_d and I_r are the disk and ring currents, respectively, and the RRDE current collection efficiency N was determined to be 0.42.

Theoretical calculations

In this study, all density functional theory (DFT) calculations were performed using the quantum ATK package, employing the Perdew-Burke-Ernzerhof (PBE) generalized gradient approximation for the exchange-correlation functions and projected augmented waves for describing electron-ion interactions¹.

The lattice parameters of the BP-Carbon model (117 C, 4 O atoms) and the Si-BP-Carbon model (116 C, 4 O atoms, 1 Si) are both $a = 11.76 \text{ \AA}$, $b = 12.71 \text{ \AA}$ and $c = 15.21 \text{ \AA}$. An energy cutoff of 500 eV and a dense Gamma-centered $4 \times 4 \times 1$ k-points grid were employed to ensure the convergence of the total energy to 10^{-5} eV and the residual forces less than 0.01 eV \AA^{-1} . The charge density difference was used to estimate the atomic charge. The ORR performances are evaluated by calculating the reaction free energy of each step.

The adsorption energies (E_{ads}) of the reaction intermediates were calculated using the following equation²:

$$E_{\text{ads}} = E_{\text{system}} - E_c - E_{\text{species}} \quad (6)$$

where E_{system} denotes the total energy of the catalyst after the intermediates are adsorbed, E_c is the catalyst's energy, and E_{species} represents the energy of the ORR intermediates.

The Gibbs free energy change (ΔG) for each step of the primitive reaction of the ORR intermediates was calculated based on the standard hydrogen electrode model³ using the following equation:

$$\Delta G = \Delta E + \Delta E_{\text{ZPE}} - T\Delta S \quad (7)$$

where ΔE denotes the reaction energy difference; ΔE_{ZPE} represents the zero-point energy difference; and T and ΔS are the temperature and entropy, respectively.

Lithium-ion battery performance testing

The experimental setup employed for lithium-ion battery testing used lithium as the cathode material, lithium hexafluorophosphate (LiPF_6) as the electrolyte, and

Celgard 2400 as the diaphragm. The working electrode was prepared by mixing the active material with carbon black and polyvinylidene fluoride in NMP at a ratio of 8:1:1 by weight. This mixture was then coated onto a copper foil and dried in a vacuum oven at 80°C for 12 h. Button cell assembly was prepared in an argon-filled glove box with moisture and oxygen levels of <1 ppm.

Charge-discharge cycling and multiplier tests were performed using a Blue Power tester, with voltage ranging from 0.005 to 3.00 V (vs. Li/Li⁺). CV and electrochemical impedance spectroscopy (EIS) were employed using a CHI 760E electrochemical tester. CV curves were obtained over a voltage range of 0.005-3.0 V at a sweep rate of 0.1 mVs⁻¹. EIS measurements were performed across a frequency range of 0.01-10⁶ Hz with a voltage amplitude of 0.005 V. The open-circuit voltage was used as the starting voltage for each cell. All electrochemical tests were performed at room temperature, with the assembled cells allowed to stabilize for 18 h before characterization.

2. Supplementary Tables

Table S1. Heteroatom-doped carbon catalysts for the ORR and their electronegativity–active site correlation.

Catalyst	Doped Heteroatom (En, C = 2.55)	Bond-Forming Way	Active Sites	Means of Proof	Transfer Electron Number	Ref.
F-doped carbon	F (3.98)	C–F	C	Expt./DFT	3.6–4.0	4
F/Cs	F (3.98)	C–F	C	Expt.	3.9	5
O-doped CNT	O (3.44)	COOH/C=O	COOH/C=O	Expt./DFT	3.0	6
O-doped CNS ₉₀₀	O (3.44)	C=O	C=O	Chemical titration strategy/DFT	2.2–2.3	7
N-doped HOPG	N (3.04)	C–N	C	CO ₂ adsorption experiments	\	8
N-doped graphene	N (3.04)	C–N	C	Selective chemical modification/DFT	\	9
I-doped graphene	I (2.66)	C–I	C	Expt.	3.86	10
P-doped graphene	P (2.19)	C–P	P	DFT	\	11
P-doped catalysts	P (2.19)	C–P/O–P	P	Expt.	3.3–3.7	12
B-doped CNTs	B (2.04)	C–B	B	Expt./DFT	2.5	13
B-doped GQD	B (2.04)	B ₄ C/ BC ₃	BC ₃	Expt./DFT	3.8	14
B, N-doped catalysts	N (3.04)/B (2.04)	C–N–B–C	B	Expt./DFT	3.9	15
F, N-doped catalysts	F (3.98)/N (3.04)	N–C–F	C	Expt./DFT	3.9	16
BP-Carbon	O (3.44)	C–O	C	Expt./DFT	2.9	This work
Si-BP-Carbon	O (3.44)/Si (1.90)	C–O–Si	Si	Expt./DFT	3.9	

Table S2. Various heteroatom-doped carbon materials for the ORR.

Catalyst	Electrolyte	Half-wave potential (V vs. RHE)	Limit current (mA cm ⁻²)	Transfer electron number	Ref.
N-self-doped carbon	0.1 M KOH	0.804	4.9	3.80	17
HMNCs	0.1 M KOH	0.704	3.5	2.70	18
N-doped CNs	0.1 M KOH	0.754	5.3	3.75–3.95	19
N-doped HLC	0.1 M KOH	0.835	6.3	3.68–3.96	20
N-doped porous carbons	0.1 M KOH	0.804	4.5–5.1	3.78–3.94	21
N-doped graphene	0.1 M KOH	0.890	5.1	3.90	22
N-doped GLC	0.1 M KOH	0.742	3.7	3.89	23
N-doped CNTs	0.1 M KOH	0.674	3.2	3.63	24
B-doped GQDs	0.1 M KOH	0.704	4.2	3.81	14
B-doped CNTs	0.1 M NaOH	0.507	8.0 mA mg ⁻¹	2.50	25
B-doped rGO	0.1 M KOH	0.710	3.0	3.69	26
S-doped graphene	0.1 M NaOH	0.650	3.8	3.89	27
S-doped graphene	0.1 M KOH	0.884	7.2	3.82	28
P-doped OMC	0.1 M KOH	0.854	5.8	3.91	29
P-doped carbon spheres	0.1 M KOH	0.744	5.7	3.86	30
N, F-doped carbon	0.1 M KOH	0.660	5.1	3.80	31
N, S-doped graphene	0.1 M KOH	0.778	5.4	3.52–3.83	32
N, S-doped GLC	0.1 M KOH	0.820	4.2	3.7–3.9	33
N, B dual-doped HCT	0.1 M KOH	0.810	4.5	3.60–4.00	34
N, P-doped biochar	0.1 M KOH	0.862	5.5	3.79–3.97	35
N, P-doped biocarbon	0.5 M KOH	0.780	4.5	3.2–3.6	36
N, P, B-doped carbon	0.1 M KOH	0.770	5.2	3.78–3.90	37
N, P, S-doped carbon	0.1 M KOH	0.820	5.2	3.81	38
BP-Carbon	0.1 M KOH	0.658	3.1	2.9	This work
Si-BP-Carbon	0.1 M KOH	0.813	4.7	3.9	

Table S3. Various heteroatom-doped carbon materials for lithium-ion batteries.

Material	Bond-Forming Way	Current density (mA g ⁻¹)	Cycle numbers	After circulation capacity (mA h g ⁻¹)	Ref.
Nitrogen-doped Regenerated Graphite	C-N	100	200	465.8	39
N-doped Carbon Fiber	C-N	1000	1000	233.6	40
B-doped carbons	B-C	0.1 C	150	340	41
N-doped porous Carbon	B-C	300	200	390	42
Cl-doped graphene	C-N	100	200	380.4	43
Br-doped graphene	C-Cl			229.5	
I-doped graphene	C-Br	250	250	210.6	43
N, S-doped porous Carbon	C-I			458	
N, S-doped Oxidized Pitch Derived Carbon	C-N/C-S	100	1000	295	44
HP-SiOC@ graphene	C-N/C-S/O-S	100	100	402.56	45
SiOC-phenyl	CO _x Si _{4-x}	1000	600	335	46
Si-CNT	CO _x Si _{4-x}	500	200	453	47
BP-Carbon	CO _x Si _{4-x}	186	120	400	48
Si-BP-Carbon	C-O	50	100	233.9	This work
	CO _x Si _{4-x}	50	100	409.4	

3. Supplementary Figures

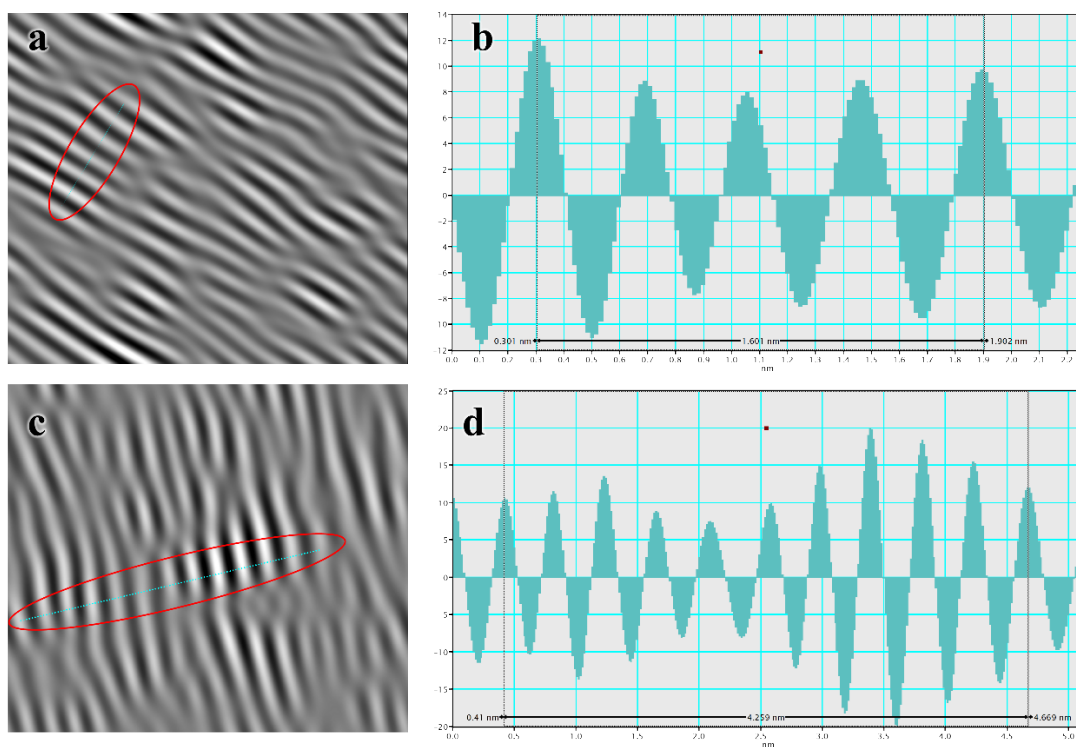


Fig. S1 a) IFFT and **b)** Live Profile of the IFFT of images of BP-Carbon; **c)** IFFT and **d)** Live Profile of the IFFT of images of Si-BP-Carbon.

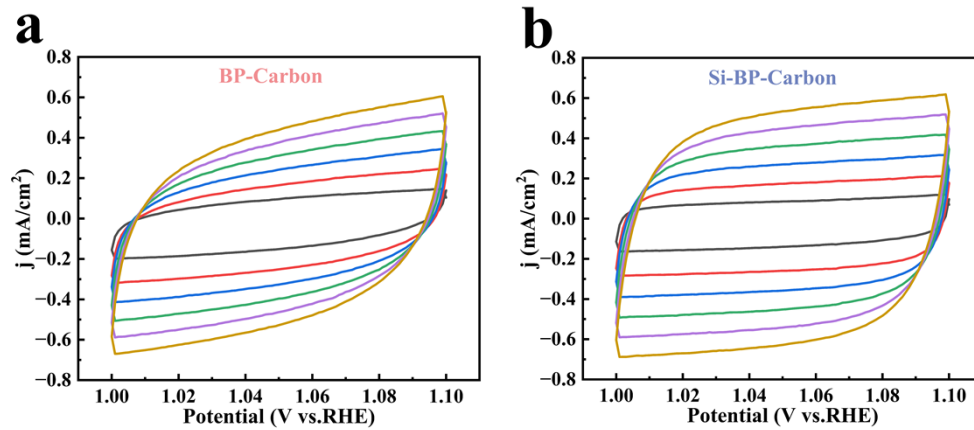


Fig. S2 Cyclic voltammograms of a) BP-Carbon and b) Si-BP-Carbon in 1.0-1.1 V N_2 -saturated 0.1 M KOH, scan rate 2, 4, 6, 8, 10, 12 $\text{mV}\cdot\text{s}^{-1}$.

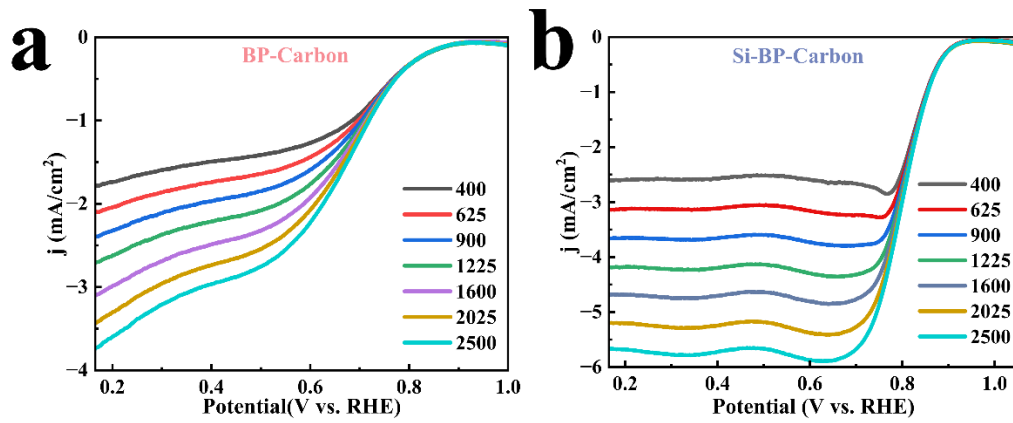


Fig. S3 a) BP-Carbon and b) Si-BP-Carbon at various rotational speeds.

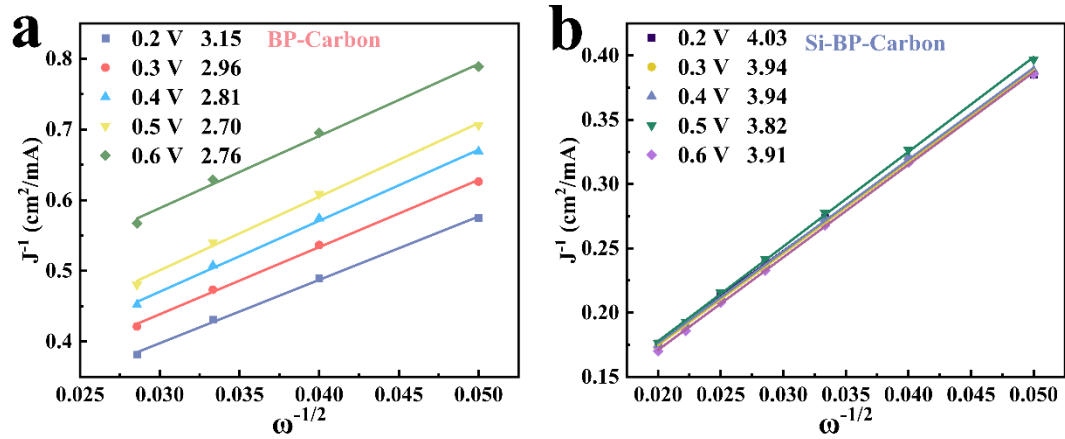


Fig. S4 K–L curves of a) BP-Carbon and b) Si-BP-Carbon.

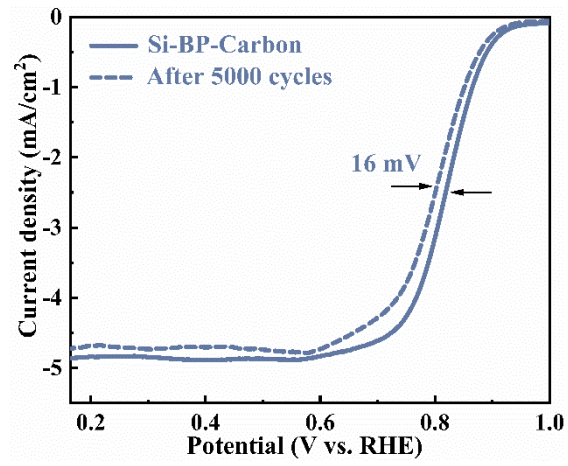


Fig. S5 LSV curve of Si-BP-Carbon before and after 5000 cycles.

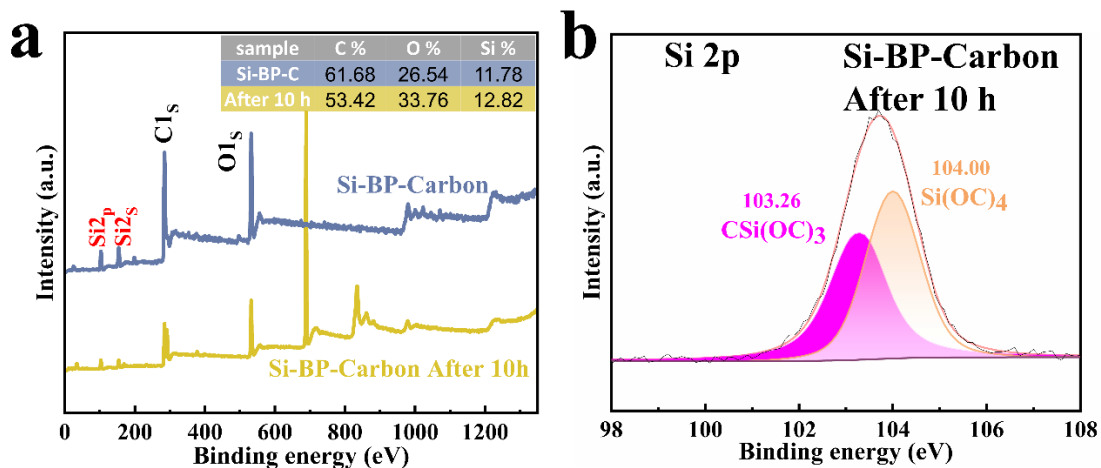


Fig. S6 XPS spectra of the Si-BP-Carbon after durability test. **a)** full spectra, **b)** Si 2p.

In Fig. S6a, the Si-BP-Carbon after the durability test exhibits peaks at 689 eV and 834 eV, corresponding to the F 1s and F Auger peaks, respectively⁴⁹. The source of the F atoms is the addition of Nafion perfluorinated resin as a binder during the preparation of the catalyst ink.

The relative content of Si atoms after the durability test did not change significantly. As XPS characterization is semi-quantitative, the relative elemental content after the durability test shows slight differences compared to the content before cycling. However, the change in Si atom content remains insignificant in relative terms.

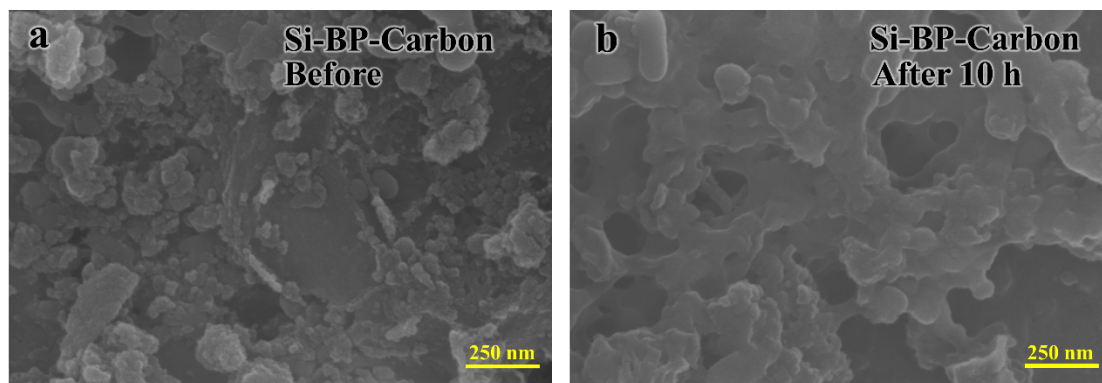


Fig. S7 SEM of Si-BP-Carbon catalyst after durability test. **a)** Before, **b)** After 10 h.

The surface of the Si-BP-Carbon catalyst becomes smooth after the durability test, likely due to the dynamic reconstruction of the surface structure during the ORR process and the deposition and rearrangement of intermediates. In addition, dissolution or desorption of weakly bound particles can occur during the ORR process, resulting in a smoother catalyst surface. Further observations show that the overall framework of the catalyst has not changed, the pores are not blocked and the surface of the catalyst has not cracked, all of which indicate that Si-BP-Carbon has good stability.

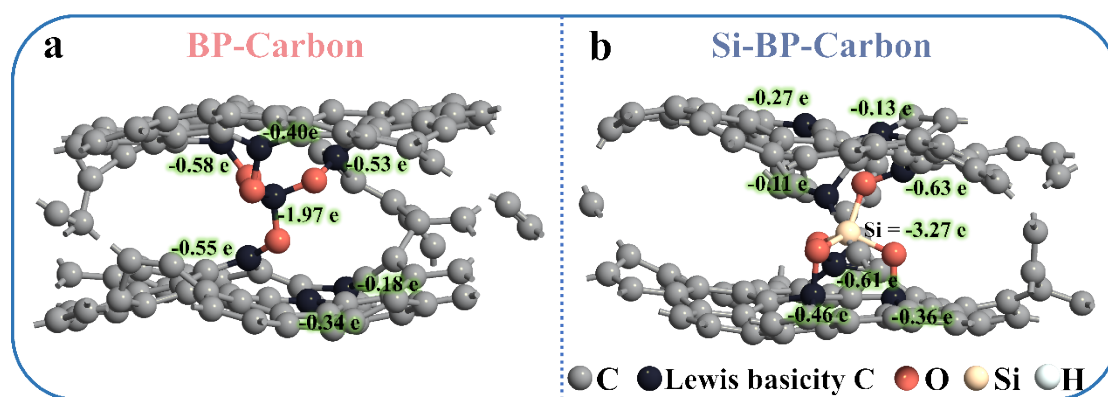


Fig. S8 Charge density difference diagrams of a) BP-Carbon and b) Si-BP-Carbon.

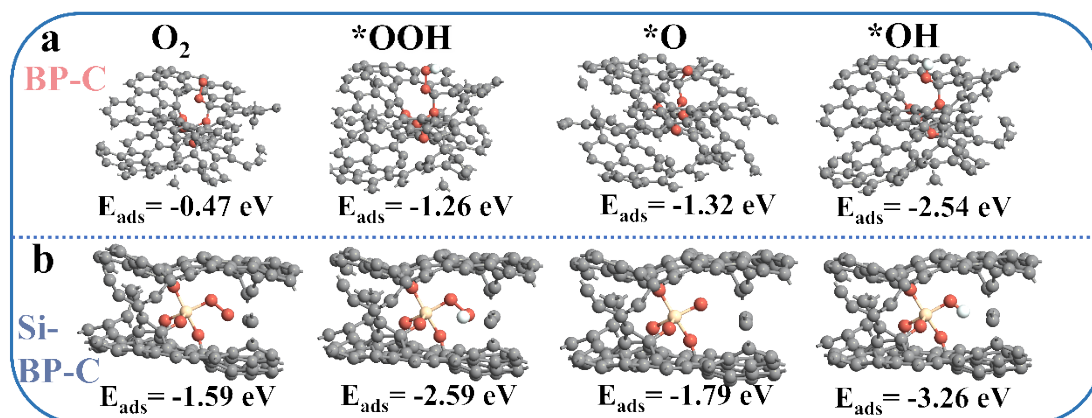


Fig. S9 Optimized configurations and adsorption energies of O₂ molecules and intermediates (*OOH, *O, *OH) on **a**) BP-Carbon and **b**) Si-BP-Carbon.

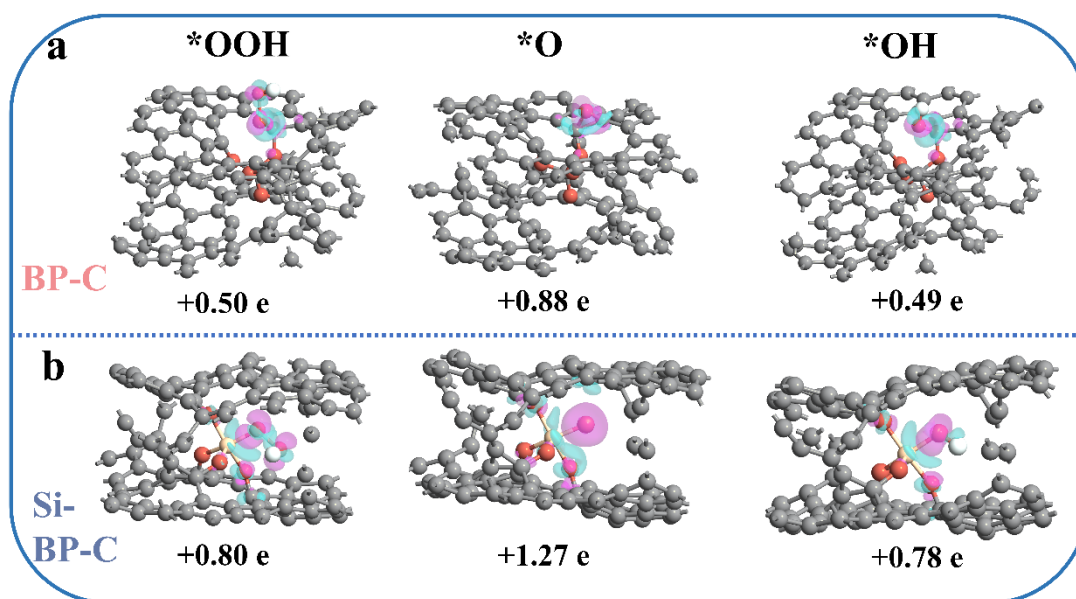


Fig. S10 Charge density difference diagrams (purple: electron accumulation; blue: electron depletion) and Bader charge transfer numbers for *OOH, *O, and *OH adsorption on **a)** BP-Carbon and **b)** Si-BP-Carbon.

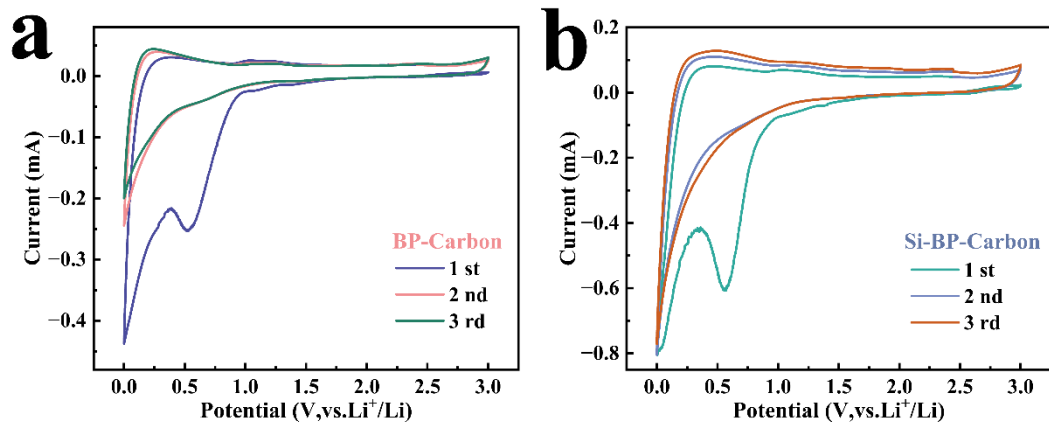


Fig. S11 Cyclic voltammety curves of a) BP-Carbon and b) Si-BP-Carbon.

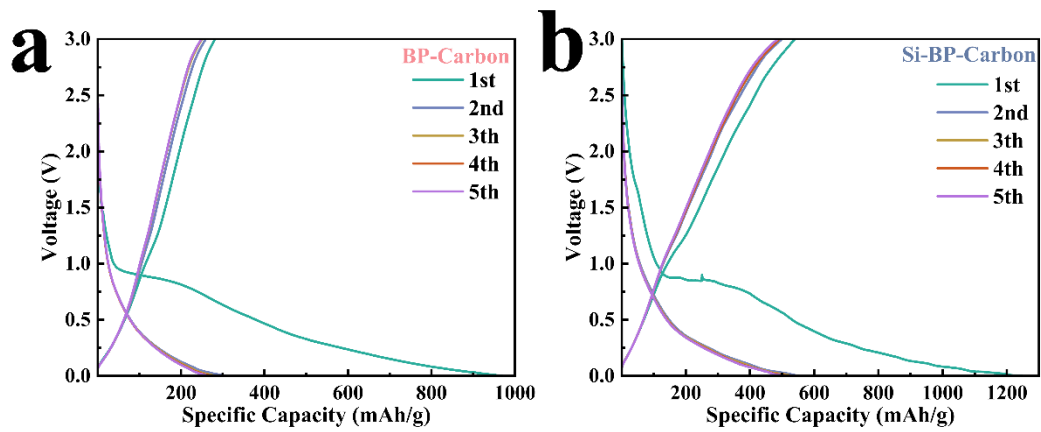


Fig. S12 Discharge and charge profiles of a) BP-Carbon and b) Si-BP-Carbon.

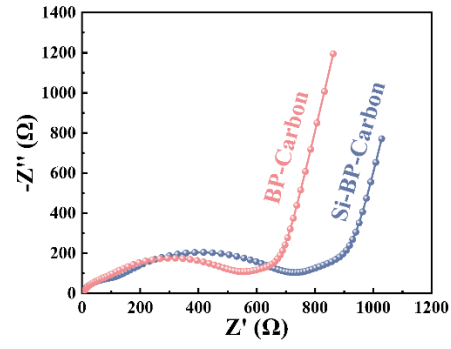


Fig. S13 Nyquist plots of BP-Carbon and Si-BP-Carbon after initial charging.

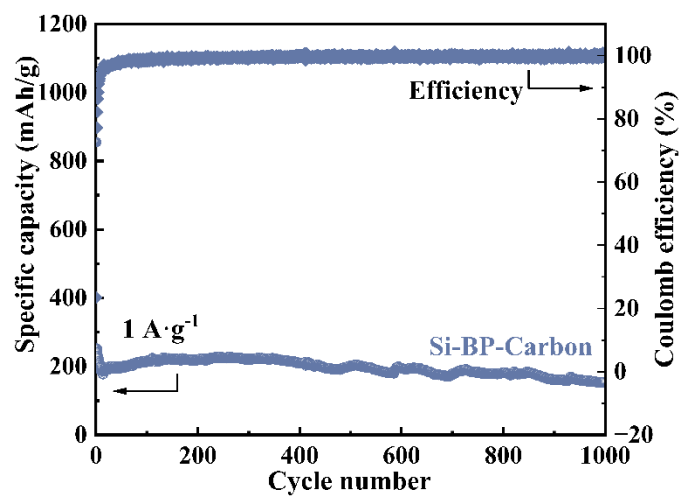


Fig. S14 Long-term cycling test of Si-BP-Carbon at current density of $1 \text{ A}\cdot\text{g}^{-1}$ for 1000 cycles.

Supporting References

1. W. Bao, Y. Tang, J. Yu, W. Yan, C. Wang, Y. Li, Z. Wang, J. Yang, L. Zhang and F. Yu, *Applied Catalysis B: Environmental*, 2024, **346**, 123706.
2. X. Chen and R. Hu, *Int J Hydrogen Energ*, 2019, **44**, 15409-15416.
3. Y. Zhang, Y. Jiang, G. Jiang, T. Or, R. Gao, H. Zhang, Z. Bai, N. Chen, Y.-P. Deng and Z. Chen, *Nano Energy*, 2023, **115**, 108672.
4. Y. Chang, J. Chen, J. Jia, X. Hu, H. Yang, M. Jia and Z. Wen, *Applied Catalysis B: Environmental*, 2021, **284**, 119721.
5. H. Wang and A. Kong, *Materials Letters*, 2014, **136**, 384-387.
6. J. Zhang, S. Qiu and F. Deng, *Journal of Hazardous Materials*, 2024, **465**, 133261.
7. S. Y. Chen, T. Luo, K. J. Chen, Y. Y. Lin, J. W. Fu, K. Liu, C. Cai, Q. Y. Wang, H. J. W. Li, X. Q. Li, J. H. Hu, H. M. Li, M. S. Zhu and M. Liu, *Angew Chem Int Edit*, 2021, **60**, 16607-16614.
8. D. H. Guo, R. Shibuya, C. Akiba, S. Saji, T. Kondo and J. Nakamura, *Science*, 2016, **351**, 361-365.
9. T. Wang, Z.-X. Chen, Y.-G. Chen, L.-J. Yang, X.-D. Yang, J.-Y. Ye, H.-P. Xia, Z.-Y. Zhou and S.-G. Sun, *ACS Energy Letters*, 2018, **3**, 986-991.
10. Z. Yao, H. Nie, Z. Yang, X. Zhou, Z. Liu and S. Huang, *Chem Commun*, 2012, **48**, 1027-1029.
11. X. Zhang, Z. Lu, Z. Fu, Y. Tang, D. Ma and Z. Yang, *Journal of Power Sources*, 2015, **276**, 222-229.
12. X. Li, Y. Qiu and P. A. Hu, *Journal of Nanoscience and Nanotechnology*, 2016, **16**, 6216-6222.
13. L. Yang, S. Jiang, Y. Zhao, L. Zhu, S. Chen, X. Wang, Q. Wu, J. Ma, Y. Ma and Z. Hu, *Angewandte Chemie*, 2011, **123**, 7270-7273.
14. T. Van Tam, S. G. Kang, K. F. Babu, E.-S. Oh, S. G. Lee and W. M. Choi, *Journal of Materials Chemistry A*, 2017, **5**, 10537-10543.
15. R. Cheng, K. Li, Z. Li, M. Jiang, F. Wang, Z. Yang, T. Zhao, P. Meng and C. Fu, *Journal of Power Sources*, 2023, **556**, 232476.
16. F. Zhang, D. Zhang, W. Liu, X. Li and Q. Chen, *Carbon*, 2022, **187**, 67-77.
17. J. Zhang, Q. Li, C. Zhang, L. Mai, M. Pan and S. Mu, *Electrochimica Acta*, 2015, **160**, 139-144.
18. G. Panomsuwan, C. Hussakan, N. Kaewtrakulchai, R. Techapiesancharoenkij, A. Serizawa, T. Ishizaki and A. Eiad-ua, *Rsc Adv*, 2022, **12**, 17481-17489.
19. R. Liu, H. Zhang, S. Liu, X. Zhang, T. Wu, X. Ge, Y. Zang, H. Zhao and G. Wang, *Physical Chemistry Chemical Physics*, 2016, **18**, 4095-4101.
20. L. Wang, S. Q. Guo, Z. Hu, B. Shen and W. Zhou, *ChemCatChem*, 2022, **14**, e202200063.
21. L. Zhang, X. Wang, R. Wang and M. Hong, *Chem Mater*, 2015, **27**, 7610-7618.
22. X. Wen, Z. Duan, L. Bai and J. Guan, *Journal of Power Sources*, 2019, **431**, 265-273.
23. D. Gu, Y. Zhou, R. Ma, F. Wang, Q. Liu and J. Wang, *Nano-Micro Letters*, 2017, **10**, 1-12.
24. Z. Chen, D. Higgins and Z. Chen, *Carbon*, 2010, **48**, 3057-3065.
25. L. Yang, S. Jiang, Y. Zhao, L. Zhu, S. Chen, X. Wang, Q. Wu, J. Ma, Y. Ma and Z. Hu, *Angewandte Chemie International Edition*, 2011, **50**, 7132-7135.

26. D. H. Min, X. Han, N. Li, M. G. Jung, S. J. Lee, H. W. Park, J. Y. Lee and H. S. Park, *Composites Part B: Engineering*, 2023, **252**, 110496.
27. J. Lee, S. Noh, N. D. Pham and J. H. Shim, *Electrochimica Acta*, 2019, **313**, 1-9.
28. Z. Yang, Z. Yao, G. Li, G. Fang, H. Nie, Z. Liu, X. Zhou, X. a. Chen and S. J. A. n. Huang, *ACS nano*, 2012, **6**, 205-211.
29. D. S. Yang, D. Bhattacharjya, S. Inamdar, J. Park and J. S. Yu, *Journal of the American Chemical Society*, 2012, **134**, 16127-16130.
30. J. Wu, C. Jin, Z. Yang, J. Tian and R. Yang, *Carbon*, 2015, **82**, 562-571.
31. D. Wu, Y. Shi, H. Jing, X. Wang, X. Song, D. Si, S. Liang and C. Hao, *Int J Hydrogen Energ*, 2018, **43**, 19492-19499.
32. I. S. Amiin, J. Zhang, Z. Kou, X. Liu, O. K. Asare, H. Zhou, K. Cheng, H. Zhang, L. Mai, M. Pan and S. Mu, *Acs Appl Mater Inter*, 2016, **8**, 29408-29418.
33. F. Zhang, J. Miao, W. Liu, D. Xu and X. Li, *Int J Hydrogen Energ*, 2019, **44**, 30986-30998.
34. C. Cao, L. Wei, Q. Zhai, G. Wang and J. Shen, *Electrochimica Acta*, 2017, **249**, 328-336.
35. L.-L. Ma, X. Hu, W.-J. Liu, H.-C. Li, P. K. S. Lam, R. J. Zeng and H.-Q. Yu, *Chemosphere*, 2021, **278**.
36. I. L. Alonso-Lemus, M. Z. Figueroa-Torres, D. Lardizabal-Gutiérrez, P. Bartolo-Pérez, J. C. Carrillo-Rodríguez and F. J. Rodríguez-Varela, *Sustainable Energy & Fuels*, 2019, **3**, 1307-1316.
37. X. Zheng, X. Cao, J. Wu, J. Tian, C. Jin and R. Yang, *Carbon*, 2016, **107**, 907-916.
38. N.-b. Huang, J.-j. Zhang, Y. Sun, X.-n. Sun, Z.-y. Qiu and X.-w. Ge, *New Journal of Chemistry*, 2020, **44**, 14604-14614.
39. C. Xu, G. Ma, W. Yang, S. Che, Y. Li, Y. Jia, H. Liu, F. Chen, G. Zhang and H. Liu, *Electrochimica Acta*, 2022, **415**, 140198.
40. Y. N. Kim, Y.-K. Lee, C. Tewari, Y. Kim, S. Lee and Y. C. Jung, *Carbon*, 2024, **221**, 118944.
41. Y. J. Chae, S. O. Kim and J. K. Lee, *J Alloy Compd*, 2014, **582**, 420-427.
42. J. Yu, C. Shi, H. Su, M. Hu, Y. Cai and Z. Li, *Journal of Materials Science*, 2023, **58**, 12258-12270.
43. J. Xu, I. Y. Jeon, J. M. Seo, S. Dou, L. Dai and J. B. Baek, *Advanced Materials*, 2014, **26**, 7317-7323.
44. W. Luo, Q. He, C. Zhang, Z. Jiang, Y. Cheng and H. Wang, *ACS Sustainable Chemistry & Engineering*, 2024, **12**, 2881-2892.
45. P. Li, P. Chen, W. Zhang, K. Kang, J. Duan, H. Wang, Q. Yuan, J. Wang and Y. Liu, *Vacuum*, 2024, **224**, 113121.
46. K. Li, G. Yuan, X. Liu, Y. Guo, R. Huang, H. Li, H. Zhang, Q. Jia, Z. Xie, S. Zhang and W. Lei, *Advanced Functional Materials*, 2023, **33**, 2302348.
47. K. Li, G. Yuan, X. Liu, Q. Xie, L. Dong, Z. Li, H. Zhang, Z. Xie, S. Zhang and W. Lei, *Energy Storage Materials*, 2024, **65**.
48. I. Z. Gonzalez, H.-C. Chiu, R. Gauvin, G. P. Demopoulos and Y. Verde-Gomez, *Mater Today*

Commun, 2022, **30**, 103158.

49. F. Gao, F. Liu, X. Bai, X. Xu, W. Kong, J. Liu, F. Lv, L. Long, Y. Yang and M. Li, *Carbon*, 2019, **141**, 331-338.